Advanced Composites and Hybrid Materials (2023) 6:113
https://doi.org/10.1007/s42114-023-00692-7

RESEARCH

Nickel nanoparticle–decorated reduced graphene oxide via one-step microwave-assisted synthesis and its lightweight and flexible composite with Polystyrene-*block*-poly(ethylene-*ran*-butylene)-*block*-polystyrene polymer for electromagnetic wave shielding application

David Skoda[1] · Jarmila Vilcakova[1,2] · Raghvendra Singh Yadav[1] · Barbora Hanulikova[1] · Tereza Capkova[1] · Marek Jurca[1] · Michal Urbanek[1] · Petr Machac[3] · Lucie Simonikova[3] · Jan Antos[1] · Ivo Kuritka[1]

Received: 3 February 2023 / Revised: 4 May 2023 / Accepted: 11 May 2023

Abstract
Nickel nanoparticle–decorated reduced graphene oxide nanocomposites (NiG) were prepared by a one-step microwave-assisted solvothermal method. The as-prepared NiG nanocomposite systems were further heated up to 800 °C under an inert atmosphere (named NiG-800) to modify their structural and electromagnetic properties. Thereafter, these developed NiG-800 nanocomposite systems of rGO and nickel nanoparticles (25 wt.%) were applied as nanofillers (50 wt.% and 70 wt.%) in a SEBS (Polystyrene-*block*-poly(ethylene-*ran*-butylene)-*block*-polystyrene) polymer matrix to create NiG-800(50)-SEBS and NiG-800(70)-SEBS nanocomposites. The addition of NiG-800 to SEBS led to an increase of Young's modulus from 16 (SEBS) to 35 MPa (NiG-800(70)-SEBS) while the maximum elongation is still around 300%. The developed NiG-800(70)-SEBS nanocomposite exhibited high-performance electromagnetic wave absorption (minimum reflection loss $RL_{min} \approx$ –48.2 dB at 9.29 GHz) at a low thickness of 2.3 mm in the frequency range of 8.2−12.4 GHz. The prepared NiG-800(70)-SEBS nanocomposite has the potential of an electromagnetic wave absorber. The NiG-800(70)-SEBS nanocomposite reported here has total shielding efficiency > 10 dB at a thickness of 1 mm in the whole frequency range (X-band) with reflection ≈ 50% and absorption ≈ 40% which has the potential for electromagnetic wave absorber applications.

Keywords Nickel · Nanoparticles · Reduced graphene oxide · Microwave synthesis · Polymer · Composite · Electromagnetic shielding

1 Introduction

In recent years, reduced graphene oxide (rGO)–based carbon nanomaterials have attracted immense research interest due to their thermal, mechanical, electronic, and optical properties and high surface area [1–5]. Reduced graphene oxide introduces the properties such as a large contact area provided by the planar structure of graphene sheets and the unique ability to promote fast electron-transfer kinetics for a variety of electroactive species [6, 7] and consequently has a high potential to be used as an electromagnetic wave absorber or shielding material [8–11]. Decorating rGO with metal nanoparticles has opened new opportunities for the preparation of advanced materials and composites [12–14]. Preparation methods, such as a hydrothermal method, for these composites involve hydrothermal reactions of nickel salts with graphene oxide (GO) followed by calcination and reduction [15, 16]. A different procedure published by Gotoh et al. [17] has introduced the preparation of Ni nanoparticle–decorated graphene sheets from cation-exchanged graphite oxide. The reaction of nickel chloride with hydrazine hydrate in GO water solution has been reported by a research group of Ji et al. [18]. Moreover, this research group further described a solvothermal

✉ David Skoda
dskoda@utb.cz

[1] Centre of Polymer Systems, Tomas Bata University in Zlin, Tr. Tomase Bati 5678, Zlin 76001, Czech Republic

[2] Department of Physics and Materials Engineering, Faculty of Technology, Tomas Bata University in Zlin, Vavreckova, 5669, 76001 Zlín, Czech Republic

[3] Department of Chemistry, Faculty of Science, Masaryk University, Kotlarska 2, Brno 61137, Czech Republic

Published online: 25 May 2023

reaction of graphite oxide with nickel acetylacetonate in triethylene glycol at 270 °C [19]. Solvothermal preparation of nickel nano-chains which were anchored on rGO has been reported by Xu et al. [20]. In addition, an interesting preparation procedure has been reported in the work of Li et al. [21]. The reported method is known as the Joule heating process and it is based on the application of direct current to the micro-Ni/rGO film mounted in a vacuum chamber. Furthermore, a facile synthesis for 3D graphene-carbon nanotube-nickel nanostructures based on the microwave decomposition of nickelocene in acetonitrile with the presence of thermally exfoliated reduced graphene oxide (TErGO) has been described by Bae et al. [22].

In recent years, electromagnetic (EM) radiation pollution has received growing attention due to its adverse effects on human health as well as on the working of electronic devices [23–29]. Therefore, high-performance electromagnetic interference (EMI) absorbing and shielding materials are required to prevent these issues [28, 30–33]. High-efficiency EM wave absorption materials for stealth technologies have also been found to escape the detection of radar effectively, which is believed to be crucial to ensure the survivability of weapons and equipment on the battlefield [25, 34]. There are three typical mechanisms involved in the development of promising EMI absorbing and shielding materials [24, 26, 34]. The first one is an interaction with the EM fields by charge carriers, which requires materials with high electrical conductivity. The second mechanism is the absorption of EM radiation by the electric and/or magnetic dipoles interacting with radiation. The third mechanism is associated with multiple internal reflections from scattering centers and interfaces or defect sites in the EM wave absorber. Hence, a nanocomposite material that combines high electrical conductivity, magnetic loss, and multiple reflections is a promising candidate for EMI absorbing and shielding [24, 26, 34]. It has already been reported that carbon-based nanomaterials containing nickel nanoparticles exhibit EMI shielding properties [35]. For example, the multiwalled carbon nanotube/nickel-coated carbonized loofah fiber/polyether ether ketone composite reported by Li et al. [36] manifested high EMI shielding efficiency. Nickel nanoparticles embedded in carbon foam or on graphene sheets have also been proposed as EMI shielding materials [37, 38]. Recently, the flexible polymer-based nanocomposite containing nickel chains for EMI shielding has been reported by Wang et al. [39]. Moreover, the epoxy matrix–based composites containing graphene and nickel nanoparticles [40] or rGO and nickel chains [41] have been reported as promising candidates for electromagnetic wave shielding applications. Recently, the metal–organic framework-derived nickel/carbon composites with optimized impedance showed potential to apply them as microwave absorbers [42]. It can be argued that nowadays the fast economical and environmentally friendly procedures for the synthesis of advanced shielding materials attracted high attention of researchers.

Herein, we report nickel nanoparticle–decorated reduced graphene oxide nanocomposite (NiG) prepared via a facile one-pot microwave solvothermal synthesis as advanced filler for flexible polymer-based composite with high electromagnetic shielding performance. The microwave-assisted reaction of graphene oxide with nickel acetylacetonate in diethylene glycol solvent with the presence dodecylamine leads to the reduction of nickel precursor and the assembling of metallic nickel nanoparticles on the reduced graphene surface. For further application in EMI shielding, the as-prepared NiG nanocomposites were annealed at 800 °C in an inert atmosphere to carbonize the material and achieve good electromagnetic properties. Carbonized NiG nanocomposites were further mixed with Polystyrene-*block*-poly(ethylene-*ran*-butylene)-*block*-polystyrene (SEBS) polymer to obtain a lightweight and highly flexible composite applicable as efficient EMI shielding material. The SEBS-based composites were prepared with 50 and 70 wt.% loadings of annealed NiG nanocomposite. It was demonstrated that the presented SEBS-based composites exhibited excellent mechanical properties and achieved high activity in EM wave absorption.

2 Experimental

2.1 Materials

Diethylene glycol (p.a., DEG), methanol (p.a.), and toluene (p.a.) were purchased from the PENTA Czech Republic. Nickel(II) acetylacetonate ($Ni(II)(Acac)_2$, 99%, $M_w = 256.91$ g mol^{-1}), SEBS copolymer (Polystyrene-*block*-poly(ethylene-*ran*-butylene)-*block*-polystyrene; $M_w \sim 89\,000$), graphite flakes (Sigma-Aldrich, product no. 332461), and dodecylamine (DDA; 98%, $M_w = 185.35$ g mol^{-1}) were purchased from Sigma-Aldrich.

2.2 Preparation of graphene oxide

Graphene oxide (GO) was prepared by a modified Hummers method [43, 44]. The typical synthesis was performed as follows: 3 g of graphite and 1.5 g of $NaNO_3$ were mixed with 75 ml of H_2SO_4 (98%) in a 1000-ml flask at 0 °C. The prepared mixture was then stirred for 15 min, and 9 g of $KMnO_4$ was carefully added to the suspension with vigorous magnetic stirring for about half an hour. Then, the prepared mixture was stirred for 30 min. After that, the reaction temperature was fixed at room temperature for an additional 48 h. Afterward, 138 ml of H_2O was added slowly to the

pasty mixture with vigorous agitation for 10 min. Then, 420 ml of warm H_2O and 30 ml of H_2O_2 were added to this prepared yellow suspension. The yellow suspension was washed with an aqueous solution of H_2SO_4 (6 wt.%) and H_2O_2 (1 wt.%). Finally, the prepared suspension was washed with deionized water until the pH was neutral.

2.3 Synthesis of nickel-decorated reduced graphene oxide nanocomposite

Graphene oxide (0.510 g) prepared via the Hummers method [43] was used and added to DEG (50 ml) in a Teflon reaction vessel (Table S1, supplementary file). Then, Ni(II) $(Acac)_2$ (0.499 g, 1.94 mmol) and dodecylamine (1.01 g, 5.45 mmol) were mixed and stirred. A teflon-lined reaction vessel containing the precursor's suspension was positioned and closed tightly in the microwave reactor. Duration of the microwave synthesis was 15 min at microwave power 100% (600 W) and temperature reached 250 °C. The details of the microwave synthesis conditions can be seen in Fig. S1 (supplementary file). Furthermore, the product solution was cooled down to 50 °C spontaneously and centrifugated and washed with methanol twice. The black precipitate was dried at 80 °C in the oven. The achieved yield of the as-prepared sample represented as NiG was 0.504 g. To investigate the impact of annealing temperature on the structural and physical characteristics, the as-prepared NiG sample was carbonized in a tubular furnace in an atmosphere of argon at 800 °C for 2 h. The carbonized nickel-decorated reduced graphene oxide nanocomposite was labeled as NiG-800.

2.4 Nickel-decorated reduced graphene oxide–based SEBS nanocomposite preparation

Nickel-decorated reduced graphene oxide–based SEBS nanocomposite, NiG-800(70)-SEBS, containing 70 wt.% of NiG-800 material was prepared as follows: 202.6 mg of NiG-800 material was mixed with 86.9 mg SEBS polymer in a beaker (Table S2, supplementary file). Then, 5 ml of toluene was added. The mixture was homogenized in an ultrasonic bath and under vigorous stirring, a black viscous solution was formed. This solution was poured into a Petri dish and left to dry in a hood at room temperature. After drying, the solid and flexible composite was obtained. In addition, the SEBS-based composite labeled as NiG-800(50)-SEBS containing 50 wt.% of the NiG-800 nanocomposite filler was prepared in the same manner as described in the case of the NiG-800(70)-SEBS.

2.5 Characterization techniques

Nickel nanoparticle–decorated rGO was synthesized in PTFE-lined microwave reactor ERTEC Magnum II (600 W; 2.45 GHz). For the product separations, EBA 21 Hettich centrifuge was used. Powder XRD patterns were recorded on Rigaku MiniFlex 600 equipped with a CoK_α ($\lambda = 1.7903$ Å) X-ray tube (40 kV, 15 mA). Data processing and crystal size calculations were done with Rigaku PDXL2 software. The average crystalline size of the crystallites was evaluated using Scherrer's formula, $d = K\lambda/\beta \cos\theta$, where d is the crystalline size, K is a grain shape–dependent constant (0.9), λ is the wavelength, θ is a Bragg reflection angle, and β is the full-width half-maximum. The heating of products was carried out in a tube furnace Nabertherm R50/250/12 with a B410 controller connected to a nitrogen atmosphere source. TGA analyses were performed on Setaram LabSys Evo with TG/DSC sensor (heating ramp 5 °C min^{-1}, up to 1000 °C, airflow 60 ml min^{-1}). SEM images were collected on Nova NanoSEM (FEI) with Schottky field emission electron source (0.02–30 keV) and TLD, and CBS detectors. Raman spectroscopy was performed on a Thermo Raman microscope Nicolet DXR equipped with a He–Ne laser with emission wavelength 633 nm (power 1 and 4 mW). The spectra were recorded from 50 to 2000 cm^{-1}. Transmission electron microscopy (TEM) was carried out on a JEOL JEM 2100 microscope operated at 200 kV (LaB_6 cathode, point resolution 2.3 Å) equipped with an OLYMPUS SYS TENGRA camera (2048 × 2048 pixels). X-ray photoelectron spectroscopy measurements were carried out on a Kratos Analytical Axis Supra spectrometer equipped with monochromatized Al-Kα radiation (1486 eV). The pressure in the analysis chamber was around 10^{-6} Pa. The analyzed area was approximately 1.4 mm^2 and the pass energy was set at 150 eV. The C 1 s peak of carbon has been fixed to 284.8 eV to set the binding energy scale [45]. The obtained data was executed with the CasaXPS program (Casa Software Ltd, UK) and spectra were deconvoluted with the least-squares fitting routine carried by the software with a Gaussian/Lorentzian (85/15) product function after subtraction of a nonlinear baseline [46]. The content of nickel in the NiG-800 nanocomposite was determined by ICP-OES spectroscopy performed on an iCAP 6500 spectrometer by Thermo Scientific (nickel spectral line $\lambda = 221.647$ nm). The complex permittivity, complex permeability, and scattering (S) parameters were measured on a PNA-L network analyzer (Agilent N5230A) using an X-band waveguide operating within the frequency range of 8.2 − 12.4 GHz. The techniques of Nicolson − Ross − Weir are utilized, which provide a direct assessment of complex permittivity and permeability using input S-parameters. The magnetization measurements were performed with a Vibrating Sample Magnetometer (Lake Shore 7407, US) at room temperature (300 K) in an air atmosphere in a magnetic field range from −760 up to + 760 kA m^{-1} (−10,000 to 10,000 Oe). The developed composites were pressed

to achieve uniform thickness for testing mechanical and shielding properties. Mechanical characteristics of SEBS nanocomposites were studied by utilizing a Testometric universal-testing machine of type M 350−5CT (Testometric Co. Ltd., Rochdale, UK).

3 Results and discussion

The nanocomposite of reduced graphene oxide (rGO) and metallic nickel nanoparticles was prepared via a one-step microwave-assisted reaction of graphene oxide and Ni(II) $(Acac)_2$ in DEG with the addition of dodecyl amine as both reduction agent and surfactant. Microwave-assisted heating was carried out in a monomodal reactor at the temperature of 250 °C for 15 min. DEG solvent was chosen due to its high permittivity (ε = 32), enabling its high dissolving capacity for polar inorganic and a variety of organic compounds [47]. An additional advantage of DEG is also its high polarizability which makes it an excellent microwave-absorbing agent [48]. The composition of the prepared NiG sample and the values of nickel content are given in Table S1 (supplementary file). The content of nickel in NiG sample determined by the ICP-OES technique was 25 wt.%.

3.1 X-ray diffraction and Raman spectroscopy

Figure 1a displays the X-ray diffraction pattern of NiG and NiG-800 samples. The observed diffraction peaks correspond to metallic nickel nanocrystals (JCPDS card no. 04–0850) and they are characteristic of the face-centered cubic (FCC) structure of nickel and indicate the (111) and (200) crystal phases [18, 49, 50]. It is worth mentioning that metallic nickel nanoparticles are already formed within a one-step MW-assisted approach which confirms that the reduction process takes place during the synthesis in the MW reactor. The apparent size of nickel crystallites contained in NiG and NiG-800 samples derived from Scherrer's formula is about 16 and 93 nm, respectively. Other intense diffraction peaks found at lower 2 theta degrees are ascribed to the GO and rGO structure [18, 49, 50]. Figure 1b depicts the Raman spectra of NiG, NiG-800, and NiG-800(70)-SEBS samples. The Raman spectra of the samples gave rise to two Raman bands around 1340 and 1587 cm^{-1}, which is indicative of the vibration modes of the disordered carbon (D-band) and in-plane vibrations (E_{2g}) of ordered graphitic carbon (G-band), respectively [18, 21, 51]. These bands are also noticed in the Raman spectra of NiG-800(70)-SEBS nanocomposite. Besides D and G bands, Raman bands for the SEBS matrix were observed around 1000 and 1450 cm^{-1}.

3.2 X-ray photoelectron spectroscopy

An X-ray photoelectron spectroscopy (XPS) was employed to thoroughly investigate the bonding relations between elements in both as-prepared NiG and NiG-800 samples. XPS survey scans over the whole binding energy region are given in supplementary information (Fig. S2, supplementary file). As displayed in the high-resolution C 1 s XPS spectrum (Fig. 2a), a major contribution is assigned to graphitic C–(C, H) groups (284.8 eV). In particular, the asymmetry of the C 1 s peak in the high binding energy (B. E.) side could be understood as the simultaneous presence of oxidized carbon species (C-O, C = O, and COO- moieties) and graphitic-like compounds,

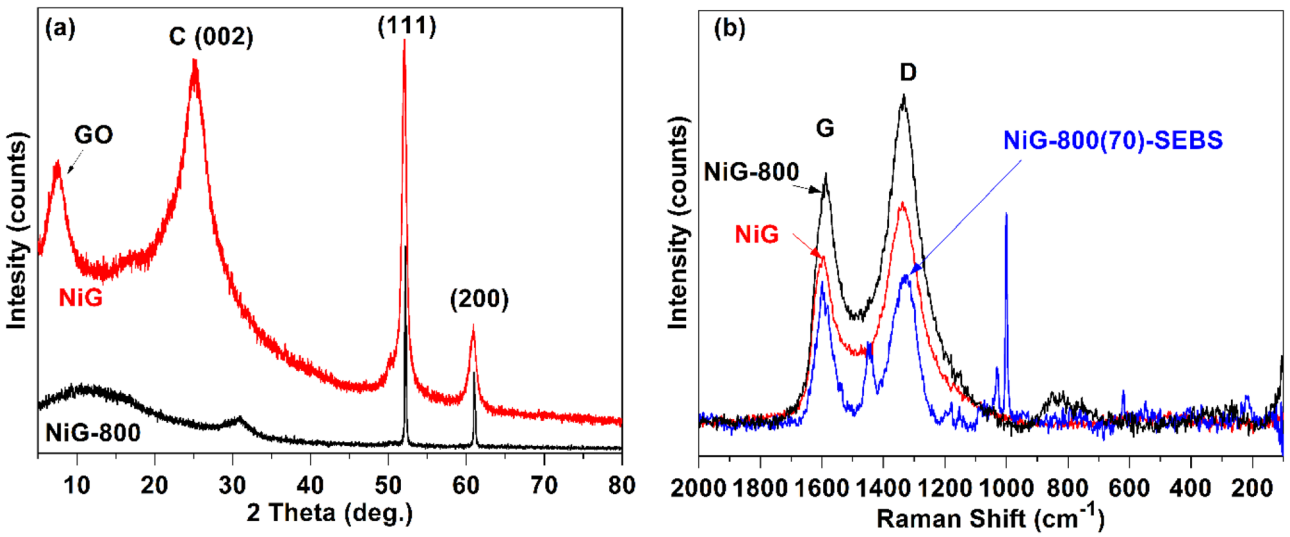

Fig. 1 **a** Powder XRD pattern of as-prepared NiG sample and NiG-800 sample using a CoK_α ($\lambda = 1.7903$ Å). **b** Raman spectra of NiG, NiG-800, and NiG-800(70)-SEBS samples

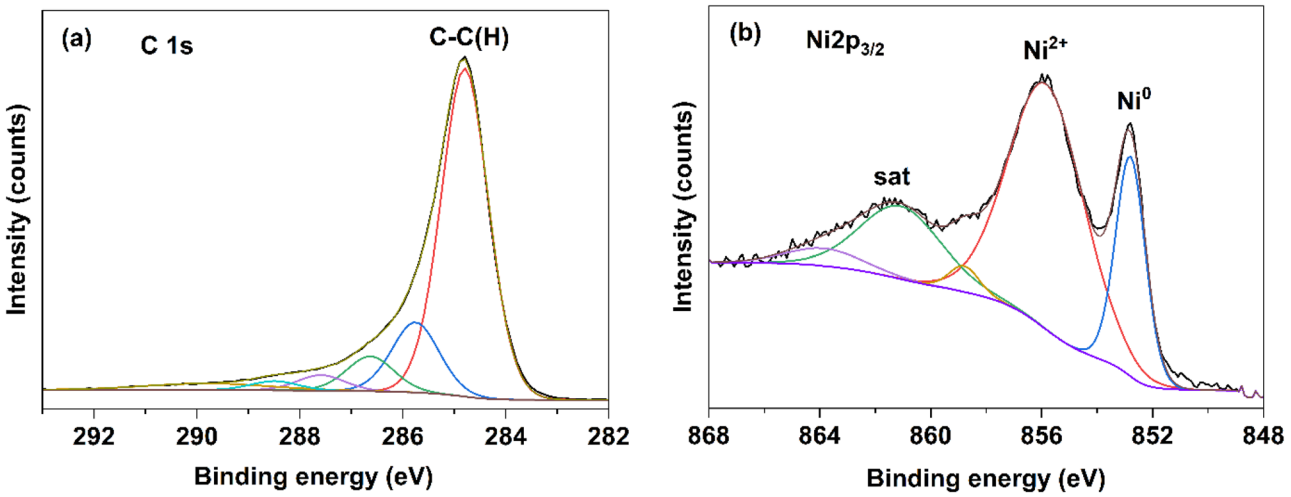

Fig. 2 **a** High-resolution C 1 s XPS spectrum of as-prepared NiG nanocomposite sample. **b** High-resolution Ni $2p_{3/2}$ XPS spectrum of as-prepared NiG nanocomposite sample

the latter presenting intrinsic asymmetry of the C 1 s peak [52–54]. The Ni $2p_{3/2}$ XPS spectrum of the as-prepared NiG sample displayed in Fig. 2b shows contributions for Ni^0 states of metallic nickel nanoparticles and Ni^{2+} states that originate from surface oxidation of nickel species or residual nickel precursor species [53, 55, 56]. In the O 1 s XPS spectrum (Fig. S3, supplementary file), the presence of Ni^{2+} species corresponds to the contribution of Ni–O species found at 529.9 eV [57]. High-resolution N 1 s XPS spectrum nitrogen exhibited the peak of amine function (Fig. S4, supplementary file) [58].

The high-resolution C 1 s XPS spectrum of NiG-800 sample is illustrated in Fig. 3a. The most intense contribution at 284.8 eV is characteristic of C–(C, H) groups of graphene or graphitic-like materials. The asymmetry of C 1 s peak in the high B. E. side could be associated with the simultaneous presence of oxidized carbon species and graphitic-like compounds [52, 54, 59]. Further, the C 1 s shoulder component with B. E. 283.3 eV could be associated with the Ni–C bond [60]. The Ni $2p_{3/2}$ XPS spectrum of NiG-800 sample (Fig. 3b) revealed contributions of Ni^0 states of metallic nickel nanoparticles and Ni^{2+} multiplet that can be assigned to oxidized surface Ni species [53, 56]. This observation correlates with the O 1 s XPS spectrum (Fig. S5, supplementary file) that shows the component of Ni–O species at 529.8 eV

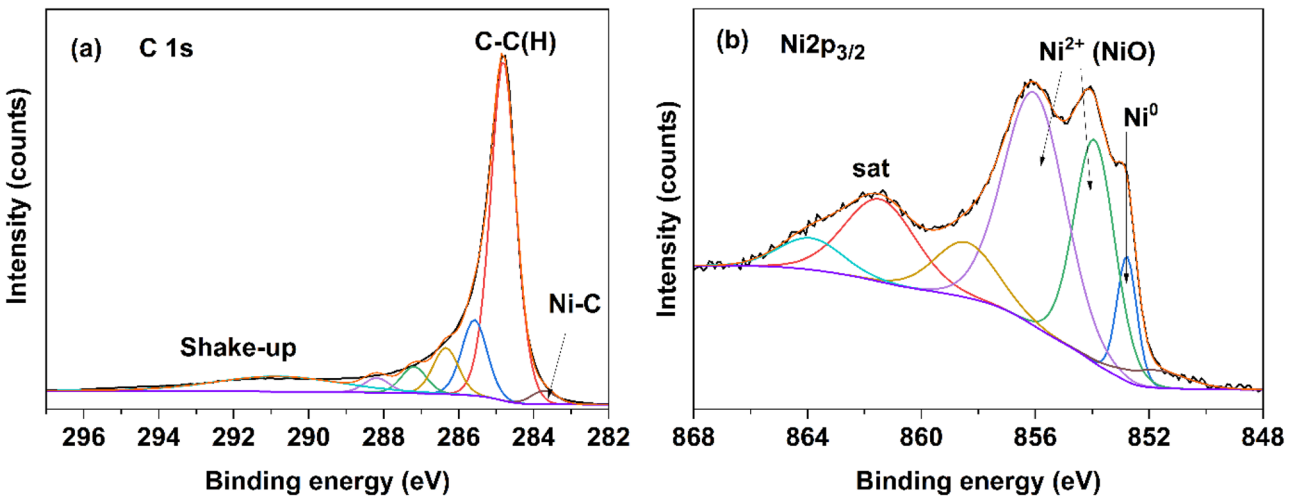

Fig. 3 **a** High-resolution C 1 s XPS spectrum of NiG-800 nanocomposite sample. **b** High-resolution Ni $2p_{3/2}$ XPS spectrum of NiG-800 nanocomposite sample

[57]. The content of nickel on the surface of NiG-800 sample determined by the XPS method is 3.3 wt.%. The N 1 s XPS spectrum (Fig. S6, supplementary file) revealed the most intense contributions of pyridinic and graphitic nitrogen atoms [54, 58]. It is proposed that nitrogen atoms are present as a consequence of dodecylamine addition within the preparation of the NiG sample.

3.3 SEM and TEM study

Figure 4 displays a scanning electron microscopy (SEM) image of NiG and NiG-800 samples. It can be noticed that the samples exhibited the morphology of rGO sheets with nickel nanoparticles embedded on the surface and between the sheet layers. Further, transmission electron microscopy (TEM) images of both NiG and NiG-800 samples, as shown in Fig. 5, revealed the structure of carbon-based nanosheets with anchored nanoparticles. It can be noticed that in the case of NiG sample, there are agglomerates of small nanoparticles (Fig. 5e), whereas the NiG-800 sample exhibited the presence of bigger, single nanoparticles of metallic nickel with the size of approximately 100 nm. This observation complements the results derived from Scherrer's formula. As illustrated in the HRTEM image in Fig. 5e, nanocrystals with lattice spacing of about 0.2 nm were observed in the case of NiG sample. This value corresponds to the (111) crystal plane of Ni nanocrystals [55]. Electron diffraction patterns of NiG and NiG-800 samples are displayed in Fig. 5f and g, respectively [61]. The content of nickel in NiG-800 nanocomposite sample determined by the SEM–EDX technique is 29.6 wt.%. It can be argued that this value corresponds to the nickel content determined by the ICP-OES method (Table S1). SEM images of NiG-800 composite with SEBS copolymer (NiG-800(70)-SEBS), as shown in Fig. 6, revealed the polymer-based matrix with incorporated NiG-800 material. The rGO-based nanosheet structures decorated with nickel particles are visible and it can be concluded that the NiG-800 nanocomposite is tightly anchored in the SEBS matrix. Based on the results from the elemental analysis of NiG-800 sample, it can be concluded that the content of nickel nanoparticles in the final composite material NiG-800(70)-SEBS is 17 wt.%.

3.4 Thermogravimetric analysis

To study the thermal behavior, TG analyses of prepared samples were performed (Fig. S7, supplementary file). TG curves of NiG and NiG-800(70)-SEBS samples recorded in

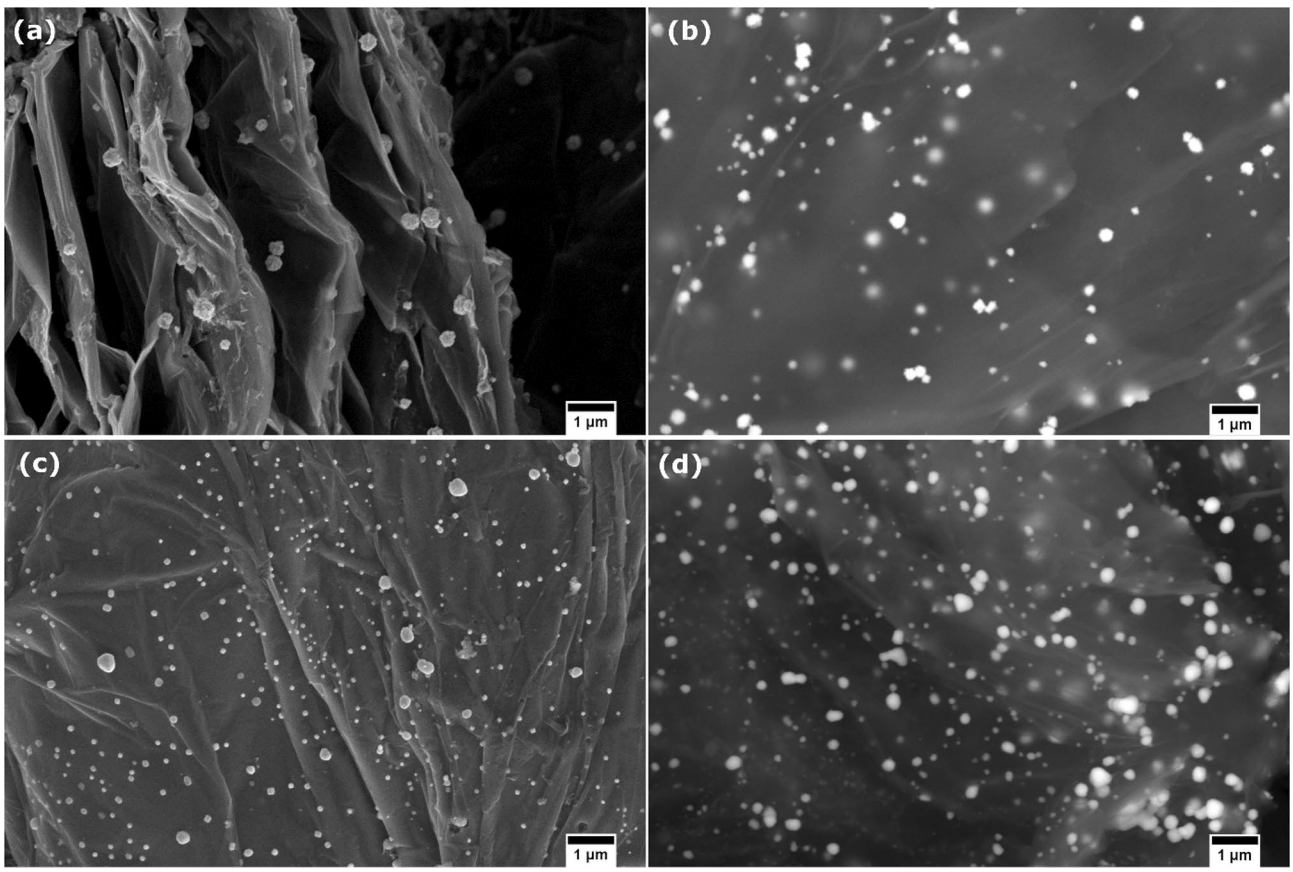

Fig. 4 SEM images of **a**, **b** NiG sample and **c**, **d** NiG-800 sample. The images (**b**, **d**) are recorded with CBS detector

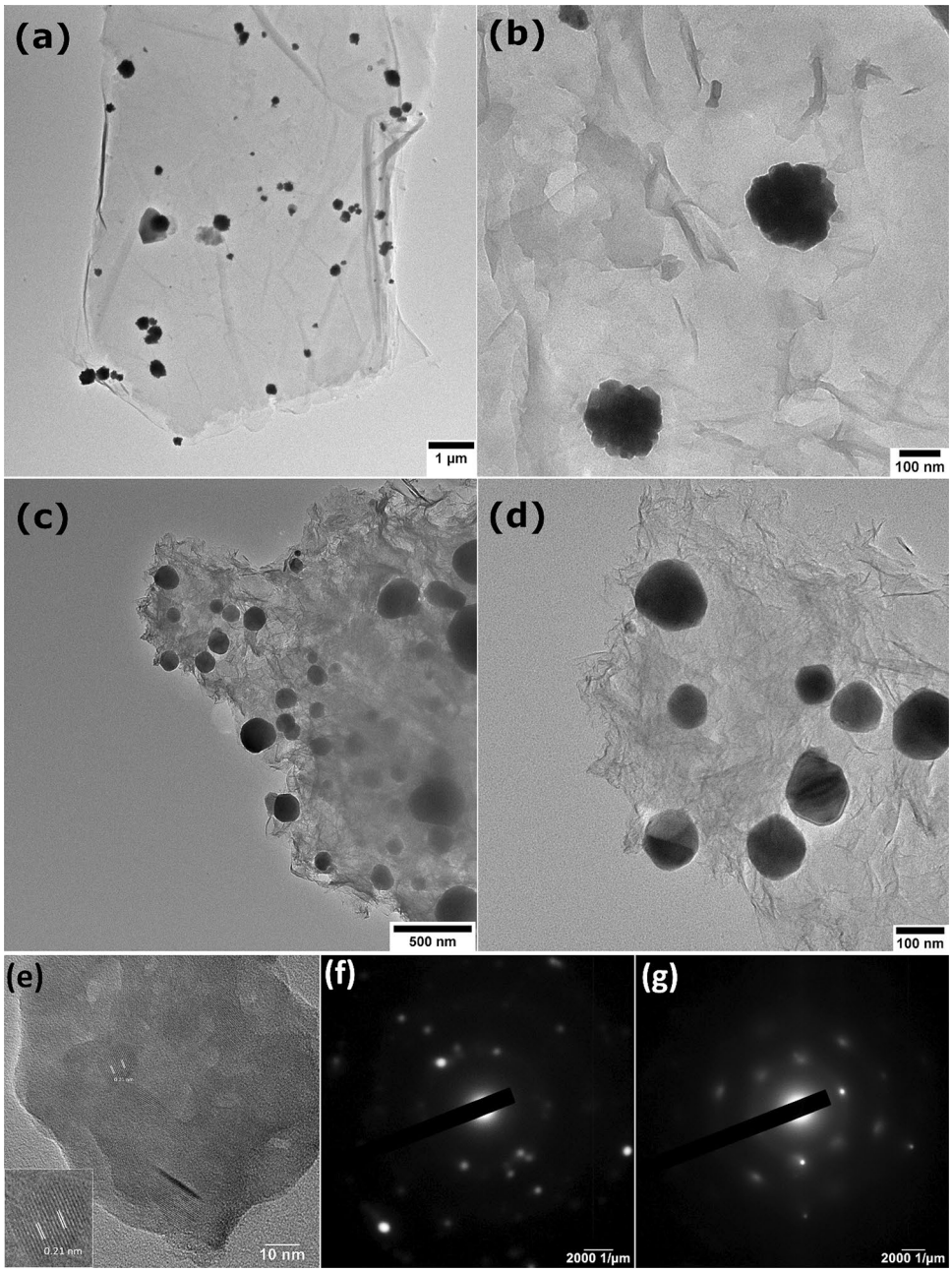

Fig. 5 TEM images of **a**, **b** NiG sample and **c**, **d** NiG-800 sample. **e** HRTEM image of NiG sample with lattice fringes corresponding to Ni (111) crystal plane. **f**, **g** Electron diffraction patterns of NiG and NiG-800 nanocomposite samples, respectively

the air atmosphere show high mass losses due to oxidation of rGO and SEBS contents. The residual mass of NiG and NiG-800(70)-SEBS sample after TG analysis performed in the air up to 1000 °C is 19.4 and 7.1%, respectively. In the case of the TG analysis of the as-prepared NiG sample performed under a nitrogen atmosphere, the residual mass was 54.3%.

3.5 Magnetic properties

The magnetic properties of the NiG and NiG-800 were investigated by utilizing a vibrating sample magnetometer (VSM) at room temperature in an applied magnetic field up to 10 kOe. Figure 7 depicts the hysteresis curves of NiG and NiG-800. The saturation magnetization values for NiG and NiG-800 nanocomposite samples are 3.41 emu g^{-1} and 8.97 emu g^{-1}, respectively. The increased value of saturation magnetization of NiG-800 nanocomposite sample is associated with an increase in crystallinity in nickel nanoparticles after annealing at high temperatures [62]. In comparison, the other reported rGO/Ni nanocomposite containing Ni nano-chains prepared from nickel chloride and hydrazine hydrate exhibited saturation magnetization values of about 3 emu g^{-1} [20]. As reported here, with the NiG and NiG-800 nanocomposites prepared via microwave-assisted approach, we achieved higher saturation

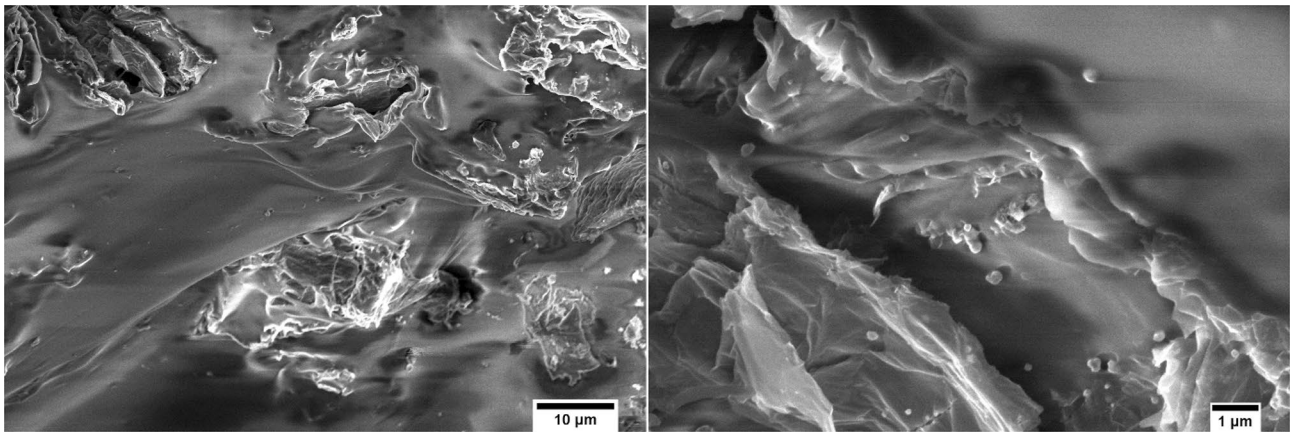

Fig. 6 SEM images of NiG-800(70)-SEBS composite sample

magnetization values. Further, the prepared NiG and NiG-800 samples display the coercivity of $H_c = 4.41$ Oe and $H_c = 3.86$ Oe, respectively. The larger M_s and lower H_c values are supportive of the enhancement of the initial permeability, which can further improve the magnetic loss and consequently EM wave absorption characteristics [63, 64]. Therefore, NiG-800 sample can provide higher EM wave absorption.

3.6 Electromagnetic interference shielding effectiveness

Electromagnetic interference shielding refers to the attenuation of the transmitting electromagnetic waves by the shielding material. A high value of electromagnetic interference (EMI) shielding effectiveness (SE) means less energy is transmitted through the shielding material. Either reflecting or absorbing the interfering electromagnetic wave will result in electromagnetic interference (EMI) shielding [65]. Although metal is the best material for electromagnetic radiation protection, the reflected wave may still interfere with the electronic component inside the enclosure or close by. Through the absorption mechanism, the electromagnetic interference shield functions on the basis that it absorbs the interfering electromagnetic wave by converting the wave energy into thermal energy and then reduces the interference to a very low value. However, absorption shielding necessitates a number of unique design requirements for the absorber's optimization, and this shielding mechanism is frequency-dependent. Measuring the portion of the incident (I_0) electromagnetic wave, transmitted (I_T) through and reflected (I_R) by the sample, scattering parameters S_{21} and S_{11}, respectively, was directly obtained as follows in Eqs. (1) and (2) [66].

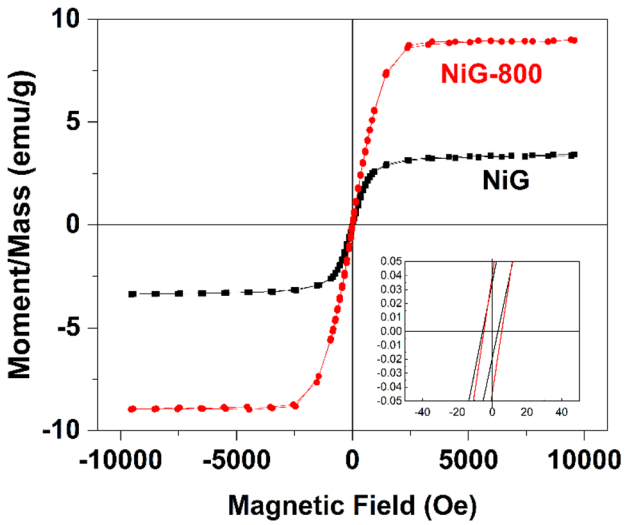

Fig. 7 Magnetic hysteresis curves of NiG and NiG-800 nanocomposites

$$S_{21}(\mathrm{dB}) = 20\log\frac{I_T}{I_0} \quad (1)$$

$$S_{11}(\mathrm{dB}) = 20\log\frac{I_R}{I_0} \quad (2)$$

While S_{11} gives a portion of reflected radiation, S_{21} provides direct information on transmitted radiation through the sample of a given thickness. The EMI shielding properties in the frequency range from 8.2 to 12.4 GHz (X-band) were determined and expressed by S_{21} parameter for the SEBS matrix as well as for concentrations 50 and 70 wt.% of NiG-800, respectively, at thickness of $t = 1$ mm, as depicted in Fig. 8. According to Fig. 8a, SEBS matrix transparency in a given region is around 94%, i.e., its shielding efficiency in a composite without nanoparticles is around $S_{21} = -0.5$ dB, which is negligible. Significantly higher shielding efficiency $S_{21} = -6$ dB was reached for nanocomposite with 50 wt.%. One of the key parameters influencing shielding efficiency

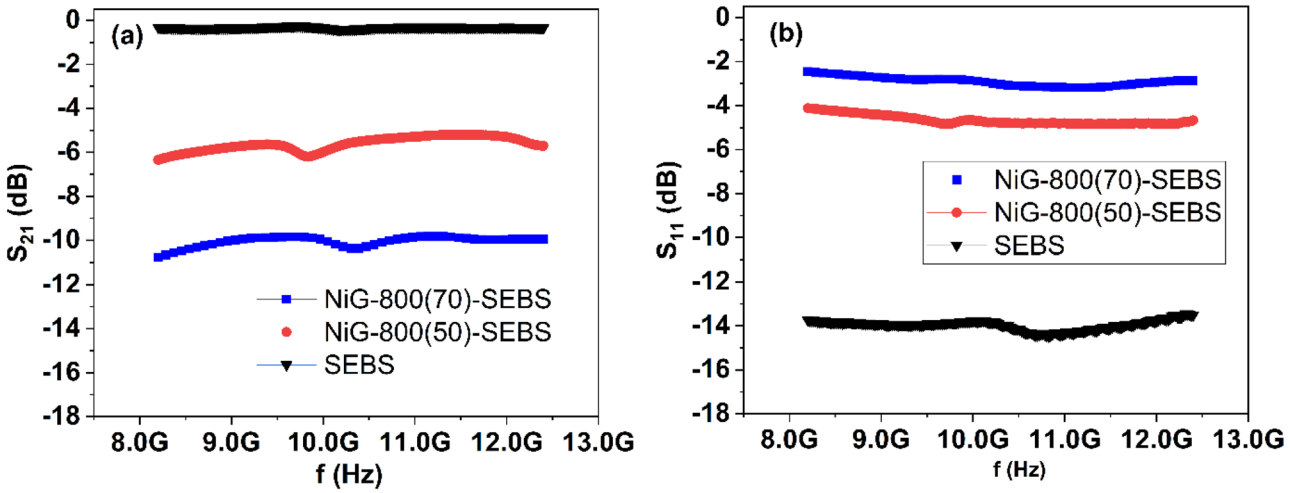

Fig. 8 Dependence of S-parameters. **a** S_{21} (dB) and **b** S_{11} (dB) on frequency

is the concentration of NiG-800 nanoparticles in the elastomer matrix. The highest achieved shielding efficiency $S_{21} = -10.6$ dB (9.8% of transparency) was obtained for NiG-800/SEBS composite containing 70 wt.% of NiG-800 sample. The increase of the S_{21} is given by the increase in conductivity which can be seen in Fig. 8b by the decrease in the value of S_{11}. The shielding efficiency of NiG-800 filled SEBS polymer samples expressed via the relationship between reflected (R), absorbed (A), and transmitted (T) portions of electromagnetic wave intensity is illustrated in Fig. S8 (supplementary file).

3.7 Reflection loss (RL)

For protection in a microwave or radio frequency band, absorbents like a microwave absorber (MAM) or a radar absorber (RAM) are used [65]. One of the most crucial requirements for microwave absorbers is that the absorbent substance minimizes front face reflection and matches the air's impedance to the absorption interface. By having high dielectric and magnetic loss values, the material must also increase the absorption of electromagnetic waves. Additionally, the dielectric properties of the material such as permittivity and magnetic properties such as permeability affect how well it absorbs electromagnetic waves. The electromagnetic proportions of these materials can be improved to achieve the maximum absorption of electromagnetic energy by incorporating dielectric and magnetic materials.

According to a generalized transmission line theory, the reflection loss (RL) can be estimated from the measured magnetic and dielectric characteristics and the radio-absorber (RA) thickness by utilizing the following equations [67, 68]:

$$RL = 20\log\left|\frac{Z - Z_0}{Z + Z_0}\right| \tag{3}$$

wherein the normalized input impedance can be calculated on the basis of the transmission line theory. When the impedance of free space and the composite material is balanced, maximum EM wave absorption implies minimum reflection loss (RL_{min}) [69–71].

To satisfy the minimum reflection loss, according to Eq. (3), the perfect matching condition is [68, 72, 73],

$$Z = j\sqrt{\frac{\mu}{\varepsilon}}\tan\left(\frac{2\pi f}{c}\sqrt{\mu^*\varepsilon^*}d\right) \tag{4}$$

Z is the input impedance of the layer; Z_0 is the wave impedance of the free space; f is the frequency; c is the speed of light; d is the layer thickness; ε^* and μ^* are complex relative permittivity and permeability. If condition $Z = 1$ is fulfilled, the reflection from the RA is absent. To find these conditions in radio-absorbing materials (RAMs), a numerical procedure close to a graphical procedure is usually applied to find the matching frequency f_0 and the matching thickness d_0 [67]. The complex permittivity (ε' and ε'') and the complex permeability (μ' and μ'') are important EM parameters for evaluating microwave absorption performance. The ε' and ε'' are related to the dielectric properties and the μ' and μ'' are associated with the magnetic properties [74].

In general, a lower RL value than −10 dB signifies the consumption of more than 90% of EM waves [75]. The reflection loss of developed nanocomposites, namely NiG-800(50)-SEBS and NiG-800(70)-SEBS, is shown in Fig. 9, in the frequency range of 8.2 to 12.4 GHz. Figure 9a

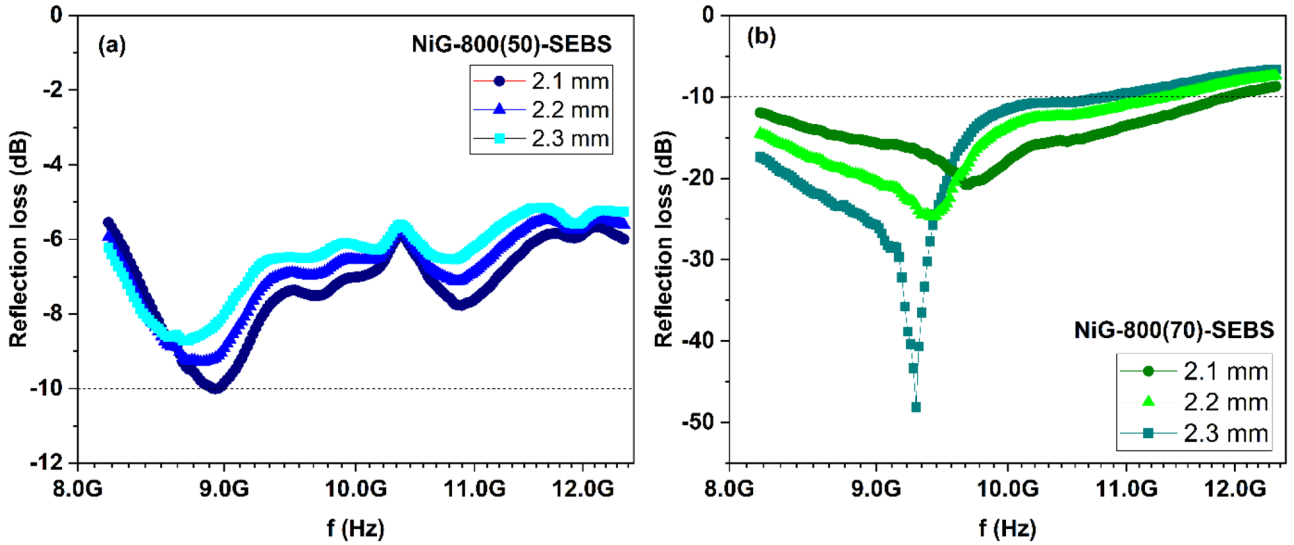

Fig. 9 Dependence RL (dB) of **a** NiG-800(50)-SEBS and **b** NiG-800(70)-SEBS on frequency and matching thickness

depicts minimum reflection loss (RL_{min}) of −10.1 dB at 8.94 GHz, −9.3 dB at 8.86 GHz, and −8.7 dB at 8.69 GHz for NiG-800(50)-SEBS at the thickness of 2.1 mm, 2.2 mm, and 2.3 mm, respectively. Further, a sharp RL peak is noticed for NiG-800(70)-SEBS nanocomposite (Fig. 9b). It displays RL_{min} of −20.6 dB at 9.67 GHz, −24.5 dB at 9.42 GHz, and −48.2 dB at 9.29 GHz for NiG-800(70)-SEBS at the thickness of 2.1 mm, 2.2 mm, and 2.3 mm, respectively. Therefore, the developed NiG-800(70)-SEBS nanocomposite exhibited excellent microwave absorption at a low thickness of 2.3 mm.

Electromagnetic parameters such as complex relative permittivity and complex relative permeability have been investigated to understand the possible electromagnetic wave absorption mechanism of the developed nanocomposites. The real part of the permittivity and permeability is associated with the storage ability of electromagnetic energy; however, the imaginary permittivity and permeability are associated with energy loss of electromagnetic energy. Figure 10a shows the real and imaginary parts of the complex relative permittivity (ε' and ε'') for developed nanocomposites. The ε' and ε'' exhibit a downward trend for both developed nanocomposites in the frequency range of 8.2 to 12.4 GHz. For NiG-800(70)-SEBS nanocomposite, the value of ε' varies from 35.8 to 26.7; however, ε'' fluctuates from 28.6 to 20.7. Further, for NiG-800(50)-SEBS nanocomposite, the value of ε' changes from 15.2 to 13.3, while, ε'' alters from 8.6 to 7.2. Various polarization behaviors, such as dipole polarization, interface polarization, and electric polarization, were linked to the fluctuation of imaginary permittivity [76]. Electric polarization could be abolished because it occurred in the 10^3–10^6 GHz frequency range. Therefore, the primary dielectric loss pathways should be the interface polarization and the dipole polarization. Interface polarization may result in a greater variation of permittivity than dipole polarization. Noteworthy, ε' and ε'' increase with an increase of NiG-800 filler content from 50 to 70 wt.% in SEBS matrix. It can be associated with the presence of high conductive reduced graphene oxide and its introduction increases with the addition of NiG-800 fillers in the SEBS matrix [77]. According to the free electron theory [78]: $\varepsilon'' = 1/2\pi\rho f\varepsilon_o$, where ρ, f, and ε_o are the resistivity, frequency, and dielectric constant of a vacuum, respectively, the improved ε'' can be attributed to increased electrical conductivity. In addition, a low value of S_{11} (−2 dB) indicates a high conductivity of the materials, which agrees with permittivities, mainly with loss part ($\varepsilon'' \approx 25$). Further, Fig. 10b shows the variation of σ_{ac} with frequency for developed NiG-800(50)-SEBS and NiG-800(70)-SEBS nanocomposites. The σ_{ac} values are in the range of 0.039–0.048 S/cm and 0.12–0.15 S/cm for NiG-800(50)-SEBS and NiG-800(70)-SEBS, respectively. To profoundly investigate the dielectric characteristics of developed nanocomposites, the relaxation mechanism, which can be expressed by the Cole–Cole semicircle, is studied. According to Debye dipolar relaxation, ε' and ε'' have the following relation (5) [78]:

$$\varepsilon' = \varepsilon_\infty + \frac{\varepsilon_s - \varepsilon_\infty}{1+(2\pi f)^2\tau^2}$$
$$\varepsilon'' = \frac{2\pi f\tau(\varepsilon_s - \varepsilon_\infty)}{1+(2\pi f)^2\tau^2} \quad (5)$$

where ε_∞ is the optical dielectric constant, ε_s is the stationary dielectric constant, f is the frequency, and τ is the relaxation time. Hence, the ε' and ε'' have the following relational expression (6) [79]:

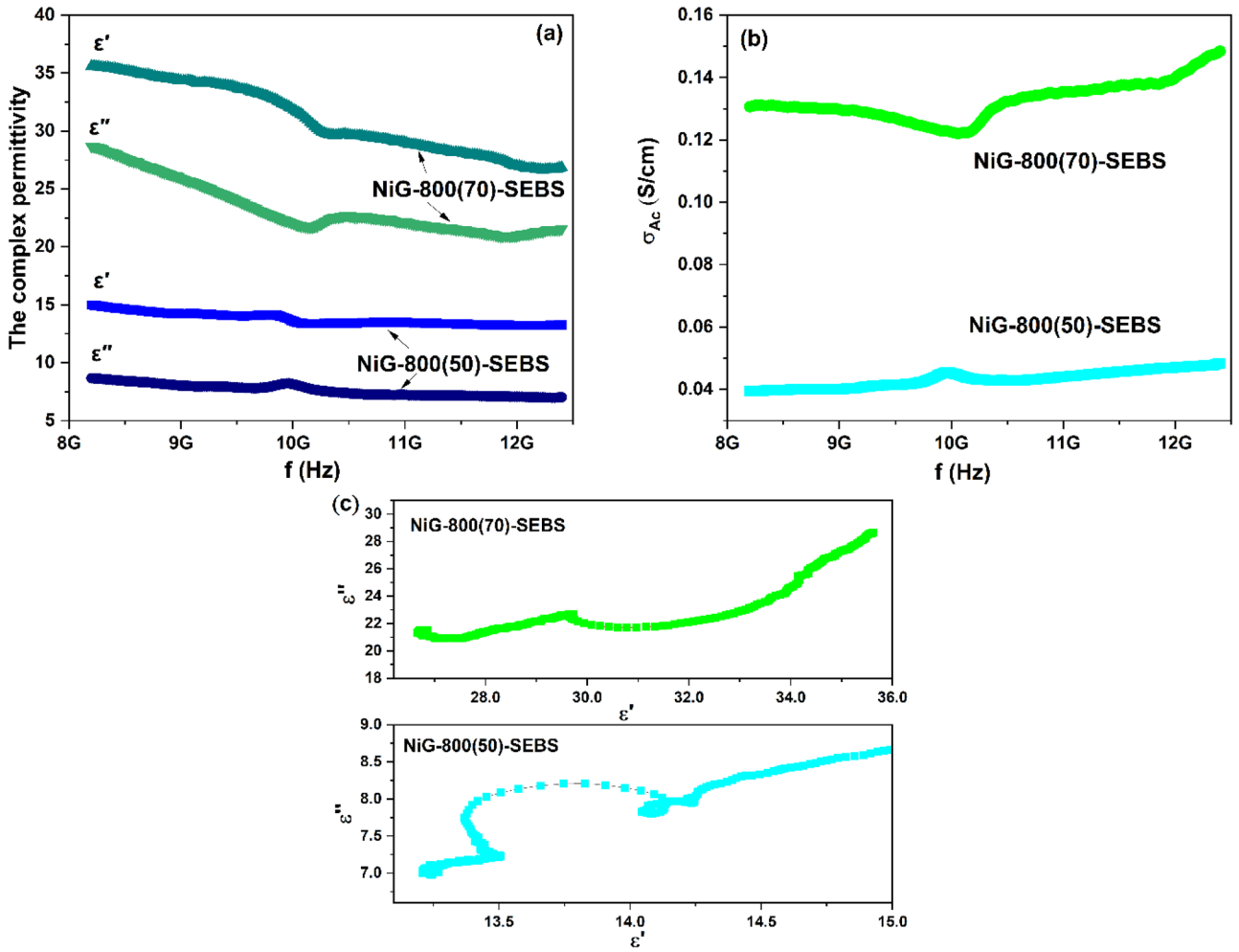

Fig. 10 Frequency dependence on **a** real and imaginary part of the complex permittivity, **b** ac conductivity, and **c** Cole–Cole plots of nanocomposites

$$\left(\varepsilon' - \frac{\varepsilon_s + \varepsilon_\infty}{2}\right)^2 + (\varepsilon^1)^2 = \left(\frac{\varepsilon_s - \varepsilon_\infty}{2}\right)^2 \tag{6}$$

Based on the above relation, the ε'- ε'' plot should be single semicircle, represented as a Cole–Cole semicircle, and every semicircle denotes one Debye relaxation process [80]. Figure 10c depicts the Cole–Cole plots of the developed NiG-800(50)-SEBS and NiG-800(70)-SEBS nanocomposites. The presence of various Cole–Cole semicircles signifies the existence of complex dipole and interfacial polarization in the developed nanocomposites [81].

Figure 11a depicts the dependence of the real part (μ') of permeability and imaginary part (μ'') of permeability of NiG-800(70)-SEBS nanocomposite. The μ' value varies in the range of 0.89–1.27 and μ'' value in the range of 0.15–0.53 for NiG-800(70)-SEBS. The dielectric loss ($\tan\delta_\varepsilon = \varepsilon''/\varepsilon'$) which signifies the dielectric loss ability of the composite material is depicted in Fig. 11b for NiG-800(70)-SEBS nanocomposite. Its value ranges from 0.69 to 0.80. Further, the magnetic loss ($\tan\delta_\mu = \mu''/\mu'$), which represents the magnetic loss ability of the material, is shown in Fig. 11c. The value of $\tan\delta_\mu$ varies in the range of 0.015–0.066 for NiG-800(70)-SEBS nanocomposite. Magnetic loss typically consists of eddy current loss, exchange resonance, and natural resonance in the GHz frequency range [82]. Nature resonance typically occurs at low frequencies, whereas exchange resonance is the main source of resonance peaks at high frequencies [83]. The two resonance peaks below 10 GHz can therefore be attributed to nature resonance, while the peak at high frequency might be the result of exchange resonances [84]. In order to further investigate the magnetic loss of NiG-800(70)-SEBS nanocomposite, the frequency (f) dependence $\mu''(\mu')^{-2}f^{-1}$ curve is studied, as shown in Fig. 11d. The $\mu''(\mu')^{-2}f^{-1}$ value remains stable or fluctuates slightly in the range of 10.1 GHz to 10.5 GHz,

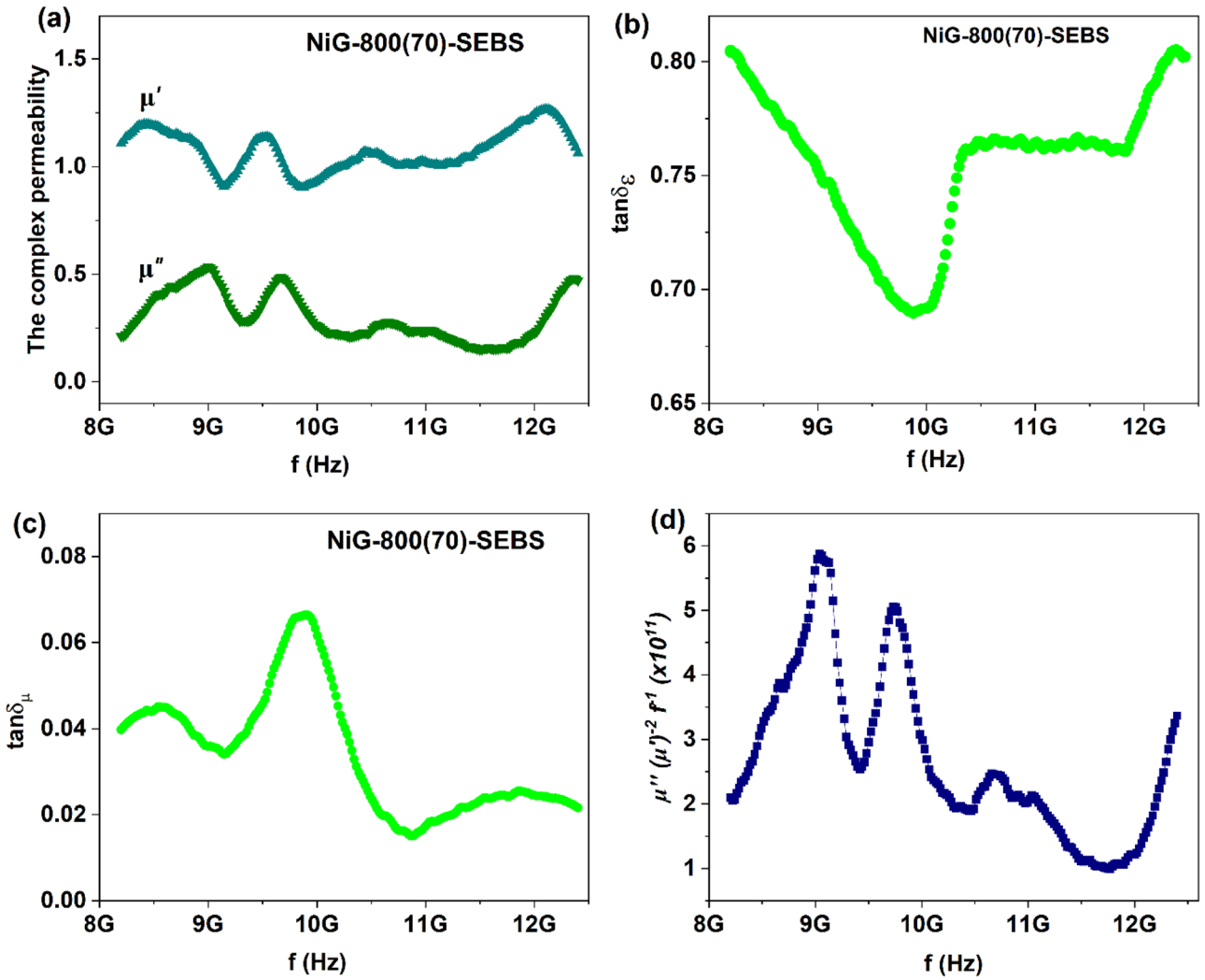

Fig. 11 Frequency dependence on **a** real and imaginary part of the complex permeability, **b** dielectric loss tangents, **c** magnetic loss tangents of NiG-800(70)-SEBS nanocomposite, and **d** $\mu''\left(\mu'\right)^{-2}f^{-1}$ of NiG-800(70)-SEBS nanocomposite

10.8 GHz to 11.0 GHz, and 11.4 GHz to 12.0 GHz, which is attributed to the eddy current loss [85]. The developed NiG-800(70)-SEBS nanocomposite exhibited a higher value of tanδ_ε in comparison with tanδ_μ, which indicates that the reflection loss is associated with an electrical loss instead of the magnetic loss [80, 86].

Figure 12 depicts an EM shielding mechanism diagram of rGO-Ni-SEBS nanocomposites. When EM wave is incident on developed nanocomposite, EM waves interact with rGO and Ni nanoparticles inside the nanocomposite [20]. The presence of rGO sheets provides the dielectric loss capability of the nanocomposites; however, Ni nanoparticles provide magnetic loss. Dipole polarization, interfacial polarization, and conductance loss can typically cause a significant dielectric loss in rGO/Ni conductive networks under the influence of alternating EM waves, consuming the EM energy. Due to the different electrical characteristics on each side of the interface, the Ni nanoparticles attached to the rGO nanosheets cause an ongoing accumulation of free charges, which causes interface polarization. During the reduction reaction, rGO nanosheets are prone to defects that result in defect dipoles. Consequently, dipole polarization occurs when the vector sum of the pole moments of the dipoles in an alternating electric field is not zero [87]. Ni nanoparticles and rGO sheets would combine to create a conductive network with finite resistance, which is advantageous to increase conduction loss and EM energy attenuation [76]. Meanwhile, under an alternating electromagnetic field, magnetic natural resonance, and magnetic exchange resonances, eddy current loss can form as a result of the action of magnetic metal Ni nanoparticles. This results in a strong magnetic loss that dissipates EM energy. The majority of the EM energy can be attenuated and transformed into thermal or other types of energy under the synergistic loss

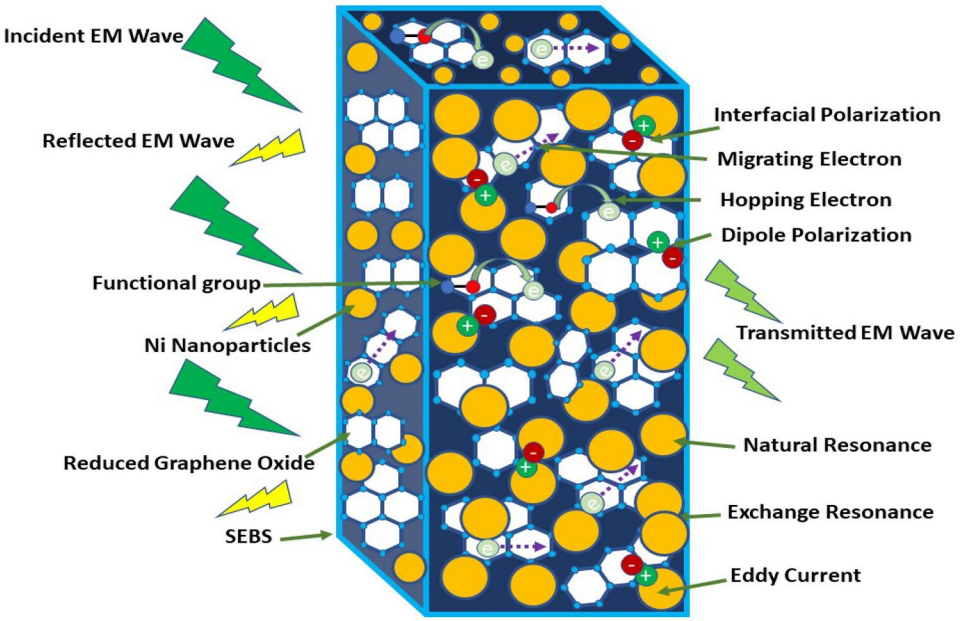

Fig. 12 EMI shielding mechanism of rGO-Ni-SEBS nanocomposites

mechanism between dielectric loss of rGO sheets and magnetic loss of Ni nanoparticles [88].

3.8 Mechanical properties

Mechanical properties of SEBS filled by NiG-800 nanoparticles were studied by tensile test as shown in stress–strain curves of NiG-800(50)-SEBS, NiG-800(70)-SEBS, and SEBS in Fig. 13. Neat SEBS polymer exhibits typical elastomeric behavior with very high maximum strain (796%) and low Young modulus (15.7 MPa). The addition of NiG-800 nanocomposite does not change the elastomeric nature of the matrix although it led to stiffening (34 MPa, 35 MPa) of the material while lowering elongation (306%, 286%) with 50 wt.% and 70 wt.%, respectively. These results show good dispersion of the filler in the matrix which agrees with Fig. 6.

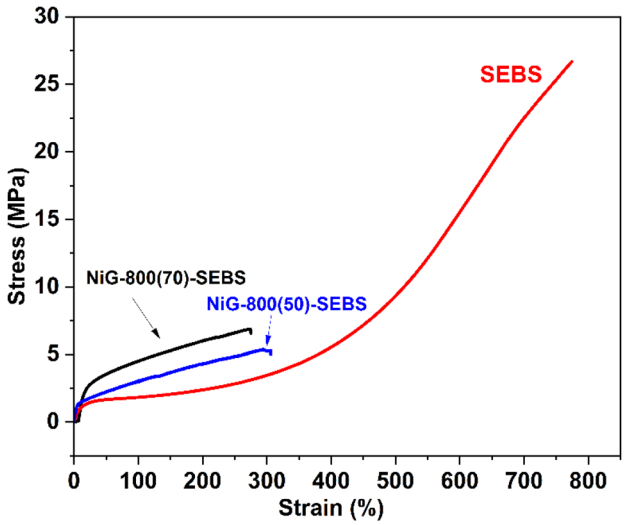

Fig. 13 Stress–strain curves of NiG-800 filled SEBS-based composites

It can be argued that the combination of nanofiller and polymer matrix properties leads to the overall performance of the material. In the case of NiG-800(70)-SEBS sample with a thickness of 1 mm, the electromagnetic properties of nickel-decorated rGO filler led to the high shielding efficiency of the composite ($S_{21} = -10.6$ dB). With the utilization of a polymer matrix based on SEBS polymer, we were able to prepare highly flexible composite material with excellent mechanical properties. There are several works describing synthesis and EM shielding properties of nickel/carbon/polymer composites [20, 35, 40, 41]. However, in these reports, epoxy resin or PVFD are used as polymer matrices. Contrary to the reported works, we developed an easy and fast approach to decorating rGO surface with nickel nanoparticles based on microwave-assisted synthesis followed by the easy incorporation of the NiG-800 nanocomposite into the SEBS polymer matrix.

4 Conclusion

SEBS-based nanocomposites consisting of nickel nanoparticle–decorated reduced graphene oxide nanocomposite particles as nanofillers (50 wt.% and 70 wt.%) were developed and investigated for EM wave shielding/absorption. Nickel nanoparticle–functionalized reduced graphene oxide nanocomposites (NiG) were prepared via one-step microwave-assisted solvothermal approach. The as-prepared

NiG nanocomposite particles were additionally annealed at 800 °C under an inert atmosphere (labeled NiG-800) to improve its structure and EM characteristics. The NiG-800 nanocomposite material contained 25 wt.% of nickel. It was demonstrated here that via mixing the NiG-800 nanocomposite with SEBS polymer we were able to easily prepare highly flexible composite material. The combination of properties of the NiG-800 nanofiller and SEBS polymer matrix resulted in the composite with promising potential for its application as EM shielding material. The prepared NiG-800(70)-SEBS nanocomposite displays minimum reflection loss $RL_{min} \approx -48.2$ dB at 9.29 GHz at a low thickness of 2.3 mm in the frequency range of 8.2 − 12.4 GHz. The total shielding efficiency of this material (thickness 1 mm) is > 10 dB in the whole frequency range (X-band) with reflection ≈ 50% and absorption ≈ 40%. Better EM wave absorption performance is achieved by the reduced graphene oxide's homogeneously distributed Ni nanoparticles and multilevel heterogeneous interfaces, which are all beneficial to the optimization of impedance matching and attenuation behavior, which further comes from the synergistic loss mechanism between dielectric loss of rGO sheets and magnetic loss of Ni nanoparticles. This research develops a quick and simple method for creating advanced nanocomposites with magnetic and dielectric components that are optimized for high-performance electromagnetic wave absorption. The present work could be beneficial in the preparation of lightweight, flexible, and high-performance EM wave absorber/shielding material.

Supplementary Information The online version contains supplementary material available at https://doi.org/10.1007/s42114-023-00692-7.

Author contribution David Skoda performed the synthesis of materials and their major characterization, wrote the main manuscript text, and reviewed the manuscript. Jarmila Vilcakova performed the electromagnetic shielding experiments, calculations, and their interpretation, and wrote the electromagnetic shielding efficiency part. Raghvendra Singh Yadav performed the calculations on electromagnetic shielding and wrote and reviewed the electromagnetic shielding part. Barbora Hanulikova performed Raman experiments and reviewed the manuscript. Tereza Capkova performed Raman experiments. Marek Jurca performed mechanical tests of the composite materials and reviewed the manuscript. Michal Urbanek performed TEM images of materials. Petr Machac performed the XPS experiments. Lucie Simonikova performed an ICP-OES analysis. Jan Antos and Ivo Kuritka reviewed the manuscript and wrote its minor parts.

Funding Open access publishing supported by the National Technical Library in Prague. This work was funded by the Ministry of Education, Youth and Sports of the Czech Republic—DKRVO (RP/CPS/2022/007), and (RP/CPS/2022/005). CzechNanoLab project LM2018110 funded by MEYS CR is gratefully acknowledged for the financial support of XPS measurements at CEITEC Nano Research Infrastructure. Masaryk University and MUNI/A/1298/2022 are acknowledged for ICP-OES analysis.

Declarations

Conflict of interest The authors declare no competing interests.

References

1. Kamat PV (2010) Graphene — a physical chemistry perspective. J Phys Chem Lett 1:587–588. https://doi.org/10.1021/jz100002j
2. Geim AK, Novoselov KS (2007) The rise of graphene. Nat Mater 6:183–191. https://doi.org/10.1038/nmat1849
3. Machado BF, Serp P (2012) Graphene-based materials for catalysis. Catal Sci Technol 2:54–75. https://doi.org/10.1039/C1CY00361E
4. Gao Y, Ma D, Wang C et al (2011) Reduced graphene oxide as a catalyst for hydrogenation of nitrobenzene at room temperature. Chem Commun 47:2432–2434. https://doi.org/10.1039/C0CC04420B
5. Chien C-T, Li S-S, Lai W-J et al (2012) Tunable photoluminescence from graphene oxide. Angew Chemie Int Ed 51:6662–6666. https://doi.org/10.1002/anie.201200474
6. Li B, Cao H, Yin J et al (2012) Synthesis and separation of dyes via Ni@reduced graphene oxide nanostructures. J Mater Chem 22:1876–1883. https://doi.org/10.1039/C1JM13032C
7. Wang J, Zhang X-B, Wang Z-L et al (2012) Rhodium–nickel nanoparticles grown on graphene as highly efficient catalyst for complete decomposition of hydrous hydrazine at room temperature for chemical hydrogen storage. Energy Environ Sci 5:6885. https://doi.org/10.1039/c2ee03344e
8. Wu C, Zeng L, Chang G et al (2023) Composite phase change materials embedded into cellulose/polyacrylamide/graphene nanosheets/silver nanowire hybrid aerogels simultaneously with effective thermal management and anisotropic electromagnetic interference shielding. Adv Compos Hybrid Mater 6:31. https://doi.org/10.1007/s42114-022-00618-9
9. Wang X, Smith P, Qiang Z et al (2022) Fire-retardant, self-extinguishing multiblock poly(esterimide)s/graphene composites with segregated structure for electromagnetic interference shielding. Compos Part A Appl Sci Manuf 163:107262. https://doi.org/10.1016/j.compositesa.2022.107262
10. Shi S, Dai M, Tao X et al (2022) 3D printed polylactic acid/graphene nanocomposites with tailored multifunctionality towards superior thermal management and high-efficient electromagnetic interference shielding. Chem Eng J 450:138248. https://doi.org/10.1016/j.cej.2022.138248
11. Jiang X, Zhao Z, Zhou S et al (2022) Anisotropic and lightweight carbon/graphene composite aerogels for efficient Ttermal insulation and electromagnetic interference shielding. ACS Appl Mater Interfaces 14:45844–45852. https://doi.org/10.1021/acsami.2c13000

12. Moussa S, Abdelsayed V, Samy El-Shall M (2011) Laser synthesis of Pt, Pd, CoO and Pd–CoO nanoparticle catalysts supported on graphene. Chem Phys Lett 510:179–184. https://doi.org/10.1016/j.cplett.2011.05.026
13. Moussa S, Siamaki AR, Gupton BF, El-Shall MS (2012) Pd-partially reduced graphene oxide catalysts (Pd/PRGO): laser synthesis of Pd nanoparticles supported on PRGO nanosheets for carbon–carbon cross coupling reactions. ACS Catal 2:145–154. https://doi.org/10.1021/cs200497e
14. Siamaki AR, Khder AERS, Abdelsayed V et al (2011) Microwave-assisted synthesis of palladium nanoparticles supported on graphene: a highly active and recyclable catalyst for carbon–carbon cross-coupling reactions. J Catal 279:1–11. https://doi.org/10.1016/j.jcat.2010.12.003
15. Bhowmik K, Mukherjee A, Mishra MK, De G (2014) Stable Ni nanoparticle–reduced graphene oxide composites for the reduction of highly toxic aqueous Cr(VI) at room temperature. Langmuir 30:3209–3216. https://doi.org/10.1021/la500156e
16. Bhowmik K, Sengupta D, Basu B, De G (2014) Reduced graphene oxide supported Ni nanoparticles: a high performance reusable heterogeneous catalyst for Kumada-Corriu cross-coupling reactions. RSC Adv 4:35442. https://doi.org/10.1039/C4RA04834B
17. Gotoh K, Kinumoto T, Fujii E et al (2011) Exfoliated graphene sheets decorated with metal/metal oxide nanoparticles: simple preparation from cation exchanged graphite oxide. Carbon N Y 49:1118–1125. https://doi.org/10.1016/j.carbon.2010.11.017
18. Ji Z, Shen X, Zhu G et al (2012) Reduced graphene oxide/nickel nanocomposites: facile synthesis, magnetic and catalytic properties. J Mater Chem 22:3471–3477. https://doi.org/10.1039/c2jm14680k
19. Ji Z, Wang Y, Shen X et al (2017) Facile synthesis and enhanced catalytic performance of reduced graphene oxide decorated with hexagonal structure Ni nanoparticles. J Colloid Interface Sci 487:223–230. https://doi.org/10.1016/j.jcis.2016.10.045
20. Xu W, Wang G-S, Yin P-G (2018) Designed fabrication of reduced graphene oxides/Ni hybrids for effective electromagnetic absorption and shielding. Carbon N Y 139:759–767. https://doi.org/10.1016/j.carbon.2018.07.044
21. Li Y, Chen Y, Nie A et al (2017) In situ, fast, high-temperature synthesis of nickel nanoparticles in reduced graphene oxide matrix. Adv Energy Mater 1601783. https://doi.org/10.1002/aenm.201601783
22. Bae SH, Karthikeyan K, Lee YS, Oh IK (2013) Microwave self-assembly of 3D graphene-carbon nanotube-nickel nanostructure for high capacity anode material in lithium ion battery. Carbon N Y 64:527–536. https://doi.org/10.1016/j.carbon.2013.08.003
23. Han Y, Lin J, Liu Y et al (2016) Crackle template based metallic mesh with highly homogeneous light transmission for high-performance transparent EMI shielding. Sci Rep 6:25601. https://doi.org/10.1038/srep25601
24. Geetha S, Satheesh Kumar KK, Rao CRK et al (2009) EMI shielding: methods and materials-A review. J Appl Polym Sci 112:2073–2086. https://doi.org/10.1002/app.29812
25. Singh AK, Shishkin A, Koppel T, Gupta N (2018) A review of porous lightweight composite materials for electromagnetic interference shielding. Compos Part B Eng 149:188–197. https://doi.org/10.1016/j.compositesb.2018.05.027
26. Yao Y, Jin S, Zou H et al (2021) Polymer-based lightweight materials for electromagnetic interference shielding: a review. J Mater Sci 56:6549–6580. https://doi.org/10.1007/s10853-020-05635-x
27. Zhang Z, Zhao Y, Li Z et al (2022) Synthesis of carbon/SiO2 core-sheath nanofibers with Co-Fe nanoparticles embedded in via electrospinning for high-performance microwave absorption. Adv Compos Hybrid Mater 5:513–524. https://doi.org/10.1007/s42114-021-00350-w
28. Cao X, Jia Z, Hu D, Wu G (2022) Synergistic construction of three-dimensional conductive network and double heterointerface polarization via magnetic FeNi for broadband microwave absorption. Adv Compos Hybrid Mater 5:1030–1043. https://doi.org/10.1007/s42114-021-00415-w
29. Li Y, Qing Y, Li W et al (2021) Novel Magnéli Ti4O7/Ni/poly(vinylidene fluoride) hybrids for high-performance electromagnetic wave absorption. Adv Compos Hybrid Mater 4:1027–1038. https://doi.org/10.1007/s42114-021-00297-y
30. Lou Z, Han H, Zhou M et al (2018) Synthesis of magnetic wood with excellent and tunable electromagnetic wave-absorbing properties by a facile vacuum/pressure impregnation method. ACS Sustain Chem Eng 6:1000–1008. https://doi.org/10.1021/acssuschemeng.7b03332
31. Zeng Z, Chen M, Pei Y et al (2017) Ultralight and flexible polyurethane/silver nanowire nanocomposites with unidirectional pores for highly effective electromagnetic shielding. ACS Appl Mater Interfaces 9:32211–32219. https://doi.org/10.1021/acsami.7b07643
32. Gao T, Ma Y, Ji L et al (2022) Nickel-coated wood-derived porous carbon (Ni/WPC) for efficient electromagnetic interference shielding. Adv Compos Hybrid Mater 5:2328–2338. https://doi.org/10.1007/s42114-022-00420-7
33. Wu Y, Huang K, Weng X et al (2022) PVB coating efficiently improves the high stability of EMI shielding fabric with Cu/Ni. Adv Compos Hybrid Mater 5:71–82. https://doi.org/10.1007/s42114-021-00401-2
34. Wang H, Li S, Liu M et al (2021) Review on shielding mechanism and structural design of electromagnetic interference shielding composites. Macromol Mater Eng 306:2100032. https://doi.org/10.1002/mame.202100032
35. Zhao B, Zeng S, Li X et al (2020) Flexible PVDF/carbon materials/Ni composite films maintaining strong electromagnetic wave shielding under cyclic microwave irradiation. J Mater Chem C 8:500–509. https://doi.org/10.1039/C9TC05462F
36. Li S, Li J, Ma N et al (2019) Super-compression-resistant multiwalled carbon nanotube/nickel-coated carbonized loofah fiber/polyether ether ketone composite with excellent electromagnetic shielding performance. ACS Sustain Chem Eng 7:13970–13980. https://doi.org/10.1021/acssuschemeng.9b02447
37. Kumar R, Kumari S, Dhakate SR (2015) Nickel nanoparticles embedded in carbon foam for improving electromagnetic shielding effectiveness. Appl Nanosci 5:553–561. https://doi.org/10.1007/s13204-014-0349-7
38. Pawar SP, Stephen S, Bose S, Mittal V (2015) Tailored electrical conductivity, electromagnetic shielding and thermal transport in polymeric blends with graphene sheets decorated with nickel nanoparticles. Phys Chem Chem Phys 17:14922–14930. https://doi.org/10.1039/C5CP00899A
39. Wang C, Gao H, Liang D et al (2022) Effective fabrication of flexible nickel chains/acrylate composite pressure-sensitive adhesives with layered structure for tunable electromagnetic interference shielding. Adv Compos Hybrid Mater 5:2906–2920. https://doi.org/10.1007/s42114-022-00482-7
40. Zhang B, Wang J, Wang T et al (2019) High-performance microwave absorption epoxy composites filled with hollow nickel nanoparticles modified graphene via chemical etching method. Compos Sci Technol 176:54–63. https://doi.org/10.1016/j.compscitech.2019.04.001
41. Gao Q, Zhang G, Zhang Y et al (2022) Absorption dominated high-performance electromagnetic interference shielding epoxy/functionalized reduced graphene oxide/Ni-chains microcellular foam with asymmetric conductive structure. Compos Sci Technol 223:109419. https://doi.org/10.1016/j.compscitech.2022.109419
42. Wu N, Zhao B, Liu J et al (2021) MOF - derived porous hollow Ni / C composites with optimized impedance matching as lightweight microwave absorption materials. Adv Compos Hybrid Mater 707–715. https://doi.org/10.1007/s42114-021-00307-z

43. Hummers WS, Offeman RE (1958) Preparation of graphitic oxide. J Am Chem Soc 80:1339–1339. https://doi.org/10.1021/ja01539a017
44. Yadav RS, Kuřitka I, Vilcakova J et al (2019) Lightweight NiFe2O4-Reduced Graphene Oxide-Elastomer Nanocomposite flexible sheet for electromagnetic interference shielding application. Compos Part B Eng 166:95–111. https://doi.org/10.1016/j.compositesb.2018.11.069
45. Jacquemin M, Genet MJ, Gaigneaux EM, Debecker DP (2013) Calibration of the X-ray photoelectron spectroscopy binding energy scale for the characterization of heterogeneous catalysts: is everything really under control? ChemPhysChem 14:3618–3626. https://doi.org/10.1002/cphc.201300411
46. Fairley N, Fernandez V, Richard-Plouet M et al (2021) Systematic and collaborative approach to problem solving using X-ray photoelectron spectroscopy. Appl Surf Sci Adv 5:100112. https://doi.org/10.1016/j.apsadv.2021.100112
47. Feldmann C (2003) Polyol-mediated synthesis of nanoscale functional materials. Adv Funct Mater 13:101–107. https://doi.org/10.1002/adfm.200390014
48. Tsuji M, Hashimoto M, Nishizawa Y et al (2005) Microwave-assisted synthesis of metallic nanostructures in solution. Chem - A Eur J 11:440–452. https://doi.org/10.1002/chem.200400417
49. Hsieh CT, Chou YW, Chen WY (2008) Synthesis and electrochemical characterization of carbon nanotubes decorated with nickel nanoparticles for use as an electrochemical capacitor. J Solid State Electrochem 12:663–669. https://doi.org/10.1007/s10008-007-0399-9
50. Veerakumar P, Chen SM, Madhu R et al (2015) Nickel nanoparticle-decorated porous carbons for highly active catalytic reduction of organic dyes and sensitive detection of Hg(II) ions. ACS Appl Mater Interfaces 7:24810–24821. https://doi.org/10.1021/acsami.5b07900
51. Gaboardi M, Bliersbach A, Bertoni G et al (2014) Decoration of graphene with nickel nanoparticles: study of the interaction with hydrogen. J Mater Chem A 2:1039. https://doi.org/10.1039/c3ta14127f
52. Kovtun A, Jones D, Dell'Elce S et al (2019) Accurate chemical analysis of oxygenated graphene-based materials using X-ray photoelectron spectroscopy. Carbon N Y 143:268–275. https://doi.org/10.1016/j.carbon.2018.11.012
53. Major GH, Fairley N, Sherwood PMA et al (2020) Practical guide for curve fitting in x-ray photoelectron spectroscopy. J Vac Sci Technol A 38:061203. https://doi.org/10.1116/6.0000377
54. Xie P, Liu Y, Feng M et al (2021) Hierarchically porous Co / C nanocomposites for ultralight high - performance microwave absorption. Adv Compos Hybrid Mater 173–185. https://doi.org/10.1007/s42114-020-00202-z
55. Wang J, Zhao Q, Hou H et al (2017) Nickel nanoparticles supported on nitrogen-doped honeycomb-like carbon frameworks for effective methanol oxidation. RSC Adv 7:14152–14158. https://doi.org/10.1039/c7ra00590c
56. Grosvenor AP, Biesinger MC, Smart RSC, McIntyre NS (2006) New interpretations of XPS spectra of nickel metal and oxides. Surf Sci 600:1771–1779. https://doi.org/10.1016/j.susc.2006.01.041
57. Zhang K, Xia X, Deng S et al (2019) Nitrogen-doped sponge Ni fibers as highly efficient electrocatalysts for oxygen evolution reaction. Nano-Micro Lett 11:21. https://doi.org/10.1007/s40820-019-0253-5
58. Kabir S, Artyushkova K, Serov A et al (2016) Binding energy shifts for nitrogen-containing graphene-based electrocatalysts – experiments and DFT calculations. Surf Interface Anal 48:293–300. https://doi.org/10.1002/sia.5935
59. Qi G, Liu Y, Chen L et al (2021) Lightweight Fe3C@Fe/C nanocomposites derived from wasted cornstalks with high-efficiency microwave absorption and ultrathin thickness. Adv Compos Hybrid Mater 4:1226–1238. https://doi.org/10.1007/s42114-021-00368-0
60. Zhang W, Li Y, Zeng X, Peng S (2015) Synergetic effect of metal nickel and graphene as a cocatalyst for enhanced photocatalytic hydrogen evolution via dye sensitization. Sci Rep 5:10589. https://doi.org/10.1038/srep10589
61. Ali M, Remalli N, Gedela V et al (2017) Ni nanoparticles prepared by simple chemical method for the synthesis of Ni/NiO-multilayered graphene by chemical vapor deposition. Solid State Sci 64:34–40. https://doi.org/10.1016/j.solidstatesciences.2016.12.007
62. Wang M, Zhou P, Feng T et al (2022) Ni-MOF/Ti3C2Tx derived multidimensional hierarchical Ni/TiO2/C nanocomposites with lightweight and efficient microwave absorption. Ceram Int 48:22681–22690. https://doi.org/10.1016/j.ceramint.2022.03.154
63. Wang C, Han X, Xu P et al (2010) Controlled synthesis of hierarchical nickel and morphology-dependent electromagnetic properties. J Phys Chem C 114:3196–3203. https://doi.org/10.1021/jp908839r
64. Xu Z, Du Y, Liu D et al (2019) Pea-like Fe/Fe 3 C nanoparticles embedded in nitrogen-doped carbon nanotubes with tunable dielectric/magnetic loss and efficient electromagnetic absorption. ACS Appl Mater Interfaces 11:4268–4277. https://doi.org/10.1021/acsami.8b19201
65. Elmahaishi MF, Azis RS, Ismail I, Muhammad FD (2022) A review on electromagnetic microwave absorption properties: their materials and performance. J Mater Res Technol 20:2188–2220. https://doi.org/10.1016/j.jmrt.2022.07.140
66. Yadav RS, Kuřitka I, Vilčáková J (2021) Advanced spinel ferrite nanocomposites for electromagnetic interference shielding applications. Elsevier
67. Lopatin AV, Kazantseva NE, Kazantsev YN et al (2008) The efficiency of application of magnetic polymer composites as radio-absorbing materials. J Commun Technol Electron 53:487–496. https://doi.org/10.1134/S106422690805001X
68. Kim SS, Jo SB, Gueon KI et al (1991) Complex permeability and permittivity and microwave absorption of ferrite-rubber composite at X-band frequencies. IEEE Trans Magn 27:5462–5464. https://doi.org/10.1109/20.278872
69. Bhattacharjee Y, Bose S (2021) Core–shell nanomaterials for microwave absorption and electromagnetic interference shielding: a review. ACS Appl Nano Mater 4:949–972. https://doi.org/10.1021/acsanm.1c00278
70. Naito Y, Suetake K (1971) Application of ferrite to electromagnetic wave absorber and its characteristics. IEEE Trans Microw Theory Tech 19:65–72. https://doi.org/10.1109/TMTT.1971.1127446
71. Gořalík M, Jurča M, Bubulinca C et al (2022) Engineering magnetic type radio-absorbers based on composites with a dual-phase polymer matrix. Electron Mater Lett 18:345–360. https://doi.org/10.1007/s13391-022-00351-x
72. Xia L, Feng Y, Zhao B (2022) Intrinsic mechanism and multiphysics analysis of electromagnetic wave absorbing materials: new horizons and breakthrough. J Mater Sci Technol 130:136–156. https://doi.org/10.1016/j.jmst.2022.05.010
73. Kim DY, Chung YC, Kang TW, Kim HC (1996) Dependence of microwave absorbing property on ferrite volume fraction in MnZn ferrite-rubber composites. IEEE Trans Magn 32:555–558. https://doi.org/10.1109/20.486547
74. Ge Y, Li C, Waterhouse GIN, Zhang Z (2021) ZnFe2O4@PDA@Polypyrrole composites with efficient electromagnetic wave absorption properties in the 18–40 GHz region. J Mater Sci 56:10876–10891. https://doi.org/10.1007/s10853-021-05968-1
75. Shen Z, Zu Y, Chen Y et al (2022) A novel synthesis method of magnetic porous carbon composites for microwave absorption. Synth Met 291:117184. https://doi.org/10.1016/j.synthmet.2022.117184
76. Li Q, Tan J, Wu Z et al (2023) Hierarchical magnetic-dielectric synergistic Co/CoO/RGO microspheres with excellent microwave

absorption performance covering the whole X band. Carbon N Y 201:150–160. https://doi.org/10.1016/j.carbon.2022.08.090
77. Li W, Liu Y, Guo F et al (2021) Self-assembly sandwich-like Fe, Co, or Ni nanoparticles/reduced graphene oxide composites with excellent microwave absorption performance. Appl Surf Sci 562:150212. https://doi.org/10.1016/j.apsusc.2021.150212
78. Sheng A, Yang Y, Yan D-X et al (2020) Self-assembled reduced graphene oxide/nickel nanofibers with hierarchical core-shell structure for enhanced electromagnetic wave absorption. Carbon N Y 167:530–540. https://doi.org/10.1016/j.carbon.2020.05.107
79. Hou M, Du Z, Liu Y et al (2022) Reduced graphene oxide loaded with magnetic nanoparticles for tunable low frequency microwave absorption. J Alloys Compd 913:165137. https://doi.org/10.1016/j.jallcom.2022.165137
80. Yi P, Yao Z, Zhou J et al (2021) Facile synthesis of 3D Ni@C nanocomposites derived from two kinds of petal-like Ni-based MOFs towards lightweight and efficient microwave absorbers. Nanoscale 13:3119–3135. https://doi.org/10.1039/D0NR07991J
81. Wang J, Wang Q, Wang W et al (2021) Hollow Ni/C microsphere@graphene foam with dual-spatial and porous structure on the microwave absorbing performance. J Alloys Compd 873:159811. https://doi.org/10.1016/j.jallcom.2021.159811
82. Cao K, Yang X, Zhang Y et al (2023) Preparation of magnetic three-dimensional porous Co-rGO aerogel for enhanced microwave absorption. Carbon N Y 208:111–122. https://doi.org/10.1016/j.carbon.2023.03.037
83. Zhao B, Fan B, Shao G et al (2015) Facile synthesis of novel heterostructure based on SnO 2 nanorods grown on submicron Ni walnut with tunable electromagnetic wave absorption capabilities. ACS Appl Mater Interfaces 7:18815–18823. https://doi.org/10.1021/acsami.5b05482
84. Quan B, Liang X, Ji G et al (2017) Cross-linking-derived synthesis of porous Co x Ni y /C nanocomposites for excellent electromagnetic behaviors. ACS Appl Mater Interfaces 9:38814–38823. https://doi.org/10.1021/acsami.7b13411
85. Cao K, Yang X, Zhao R, Xue W (2023) Fabrication of an ultralight Ni-MOF-rGO aerogel with both dielectric and magnetic performances for enhanced microwave absorption: microspheres with hollow structure grow onto the GO nanosheets. ACS Appl Mater Interfaces 15:9685–9696. https://doi.org/10.1021/acsami.2c22935
86. Zhu Z, Sun X, Li G et al (2015) Microwave-assisted synthesis of graphene–Ni composites with enhanced microwave absorption properties in Ku-band. J Magn Magn Mater 377:95–103. https://doi.org/10.1016/j.jmmm.2014.10.079
87. Sun M, Lu X, Gao H et al (2022) Lightweight porous carbon/rGO/Ni chain composite with excellent microwave absorption performance and multi-functional properties. Synth Met 291:117208. https://doi.org/10.1016/j.synthmet.2022.117208
88. Han G, Ma Z, Zhou B et al (2021) Cellulose-based Ni-decorated graphene magnetic film for electromagnetic interference shielding. J Colloid Interface Sci 583:571–578. https://doi.org/10.1016/j.jcis.2020.09.072